Consideration of Experiment to Introduce MEMS Devices into Spectroscopic Systems for Bending and Three-point Tension Tests

Akinobu Yamaguchi,[1,4]* Takuo Ohkochi,[2,3,4] Masaki Oura,[4]
Tokuji Yokomatsu,[5] and Kensuke Kanda[5]

[1]Department of Electrical, Electronic and Communications Engineering, Faculty of Science and Engineering, Toyo University, 2100 Kujirai, Kawagoe-city, Saitama 350-8585, Japan
[2]Laboratory of Advanced Science and Technology for Industry, University of Hyogo, 3-1-2 Kouto, Kamigori, Hyogo 678-1205, Japan
[3]Japan Synchrotron Radiation Research Institute, 1-1-1 Koto, Sayo, Hyogo 679–5198, Japan
[4]RIKEN SPring-8 Center, 1-1-1 Kouto, Sayo-gun, Hyogo 679–5148, Japan
[5]Graduate School of Engineering, University of Hyogo, Shosha, Himeji, Hyogo 671-2280, Japan

Recently, material strength measurements have been often performed by combining mechanical material characterization and lattice diffraction experiments using hard X-rays. When X-ray diffraction experiments are performed simultaneously with tensile tests, plastic deformation due to stress can be analyzed at the lattice level. Although this evaluation procedure is suitable for materials such as metals, it does not provide information on molecular state changes and stress-induced electronic state transitions in polymer materials. Combined with an evaluation system in the electron energy band involved in chemical bonding during the tensile stress application, the systems would advance our understanding of adhesion states such as interfaces in polymer materials and composites. Here, we developed a MEMS-based system aimed at implementing a Raman spectroscopy imaging system and a stress control system on a soft X-ray absorption spectroscopy and photoelectron spectroscopy microscopy (PEEM) system. We prepared two types of MEMS device: a double-sided beam structure device and a three-point tensile testing device. A three-point tensile MEMS was integrated into a micro-Raman spectroscopy system to perform micro-Raman spectroscopy measurements during the tensile testing of a silicon beam. As for the double-sided beam structure MEMS, it was successfully introduced into the synchrotron radiation PEEM system and its operation was confirmed in vacuum.

1.   Introduction

In recent years, there have been many reports on the creation of novel materials such as graphene[1] and topological insulators[2] that are very interesting and have potential applications

---

in low dimensions. Graphene, in particular, is a material that is expected to become a beyond-CMOS material, and there are reports of field-effect transistors fabricated from graphene.[3–5] However, it is difficult to modulate its electronic structure and express functionality by carrier doping as freely as in semiconductor devices. Particularly in silicon-based semiconductors, where purity can be guaranteed down to eleven nine (11N), carrier concentration control and band structure control work very effectively. In compound semiconductors, the band structure can be controlled by crystal growth using artificial lattices and thin-film growth, which has enabled the development of high-frequency devices such as high-electron- mobility transistors.[6] On the other hand, silicon-based semiconductors are very important devices in terms of both cost and process, but the limits of device performance due to advances in microfabrication and the band structure itself are becoming apparent. Therefore, in SiGe-based semiconductor devices,[7] a band modulation mechanism based on lattice distortion has been introduced to achieve high carrier mobility. This active use of lattice distortion has the potential not only to modulate the band structure of known material systems, but also to express new functionalities, and the smallest mutation in nanospace has the potential to alter the properties of the entire material system on a macroscopic scale.[8–13]

For example, elastic modulus is treated as a well-known material constant on a macroscopic level, but from a microscopic view point, it is expressed by crystal lattice and electron correlation.[8–19] For example, the elemental substitution or application of external stress induces band modulation, which changes the physical properties of materials, and this physical property change has been studied by various methods to pursue scientific theories. For example, rare-earth compounds including Ce exhibit a transition to superconductivity at low temperatures when pressure is applied.[20,21] This phenomenon is caused by the modulation of electronic correlations on the nano- and microscales by macroscopic pressure effects, and has been clarified by precisely measuring macroscopic response characteristics with high sensitivity using the de Haas–van Alphen and magnetoresistance effects, which directly enable us to observe the Fermi surface.[20,21] The theoretical description of the microscopic picture using physical models has revealed various physical symmetries and origins behind the phenomenon, leading to the rediscovery of two-dimensional materials such as graphene.[8,9]

In fact, the mechanisms of adhesion, friction, rubbing, degradation, destruction, cohesion, and dispersion are not well understood. This is because the physical and chemical phenomena at interfaces and surfaces are occured at the boundaries between different materials. Interfaces and surfaces are often ignored in the bulk. However, in nanoscale and microscale materials and devices, the effects of interfaces and surfaces are more pronounced.[10,22–24] Nanoscale materials are all around us if we are aware of them. For example, the permanent magnet materials used in motors and generators are made of sintered nano/microparticles, and recent studies have shown that the magnetic properties of the nano/microparticles themselves and the composition of elements and structures at their grain boundaries determine their magnetic properties. In addition, gold colloids are used for stained glass because their color changes with the particle size, and by modifying their surfaces with antibodies, they are used as a labeling and display mechanism in immunochromatography, and are widely used in medical settings as kits for testing for infectious diseases.[25,26] Antigen–antibody reactions are chemical bonding reactions at the interface, with liquid as the surrounding environment. The mechanism of action and the

electronic state at such sites are still largely unknown.

In view of the above, it is essential to elucidate the governing factors and mechanisms of action of nano- and microscale mechanical properties in order to understand the fundamental physical and chemical mechanisms. For this purpose, a system that can measure electronic states and chemical bonding at surfaces and interfaces while controlling mechanical specifics in a microregion is demanded.[23,24]

Therefore, in this study, we focused on micro electro mechanical systems (MEMS) devices, whose mechanical behavior can be controlled by electrical stimuli and vice versa.[16,17,27–30] Synchrotron radiation analysis is a very powerful analytical tool, but especially for soft X-ray analysis, devices must be manipulated in vacuum, and it is difficult to introduce ordinary mechanical tensile testing machines and actuators into a vacuum chamber. Therefore, as schematically illustrated in Fig. 1(a), we will construct an experimental system to perform synchrotron radiation analysis and micro-Raman spectroscopy measurements using MEMS devices.

2.   Experimental Procedure

MEMS design was conducted to realize MEMS devices for in-plane three-point tensile test and out-of-plane bending deformation, schematically illustrated in Fig. 2 and Fig. 3, respectively.
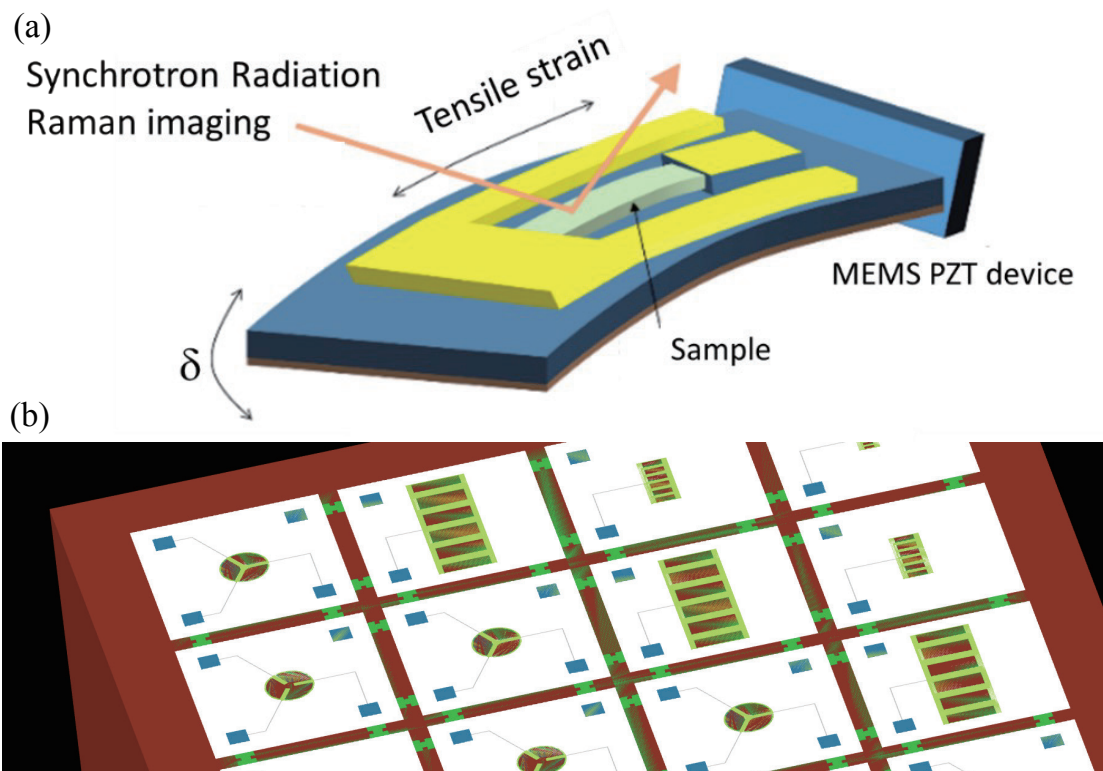

Fig. 1.   (Color online) (a) Schematic of synchrotron radiation analysis and Raman spectroscopy for a sample strained by using MEMS device. (b) Layout of MEMS device on silicon wafer generated from CAD data.
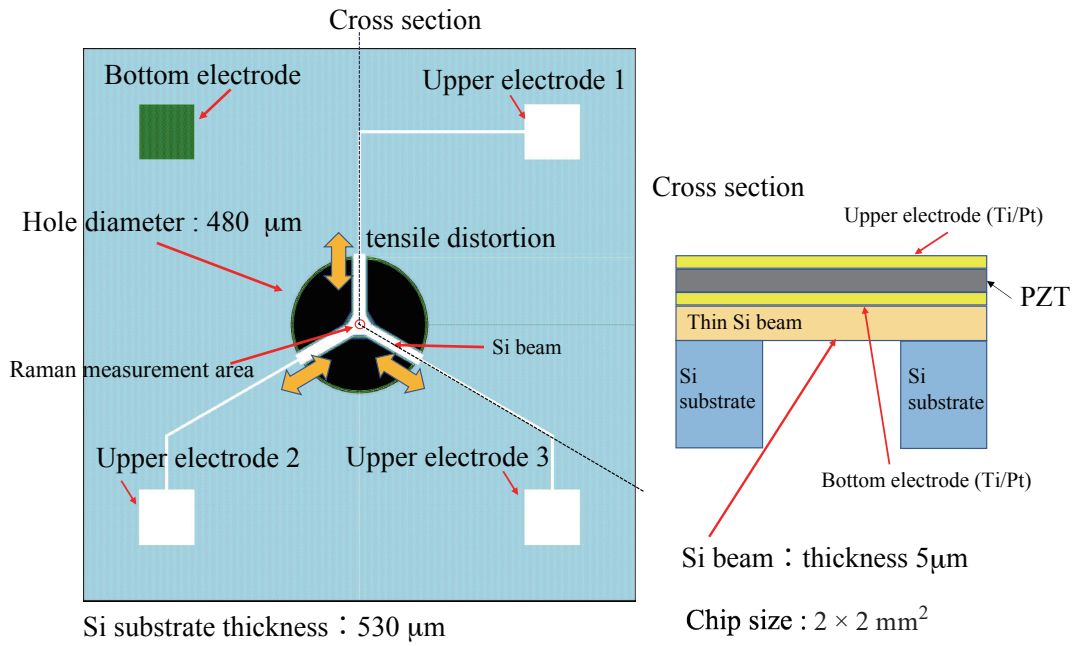
Fig. 2.   (Color online) Overview of a three-point tensile test MEMS device. The substrate size is 2×2 mm^2. The three-point tensile test mechanism structure is located at the center. The silicon island at the center is strained by PZT in three directions and subjected to tensile or compressive stress. A schematic of the MEMS cross-sectional shape is shown in the inset.
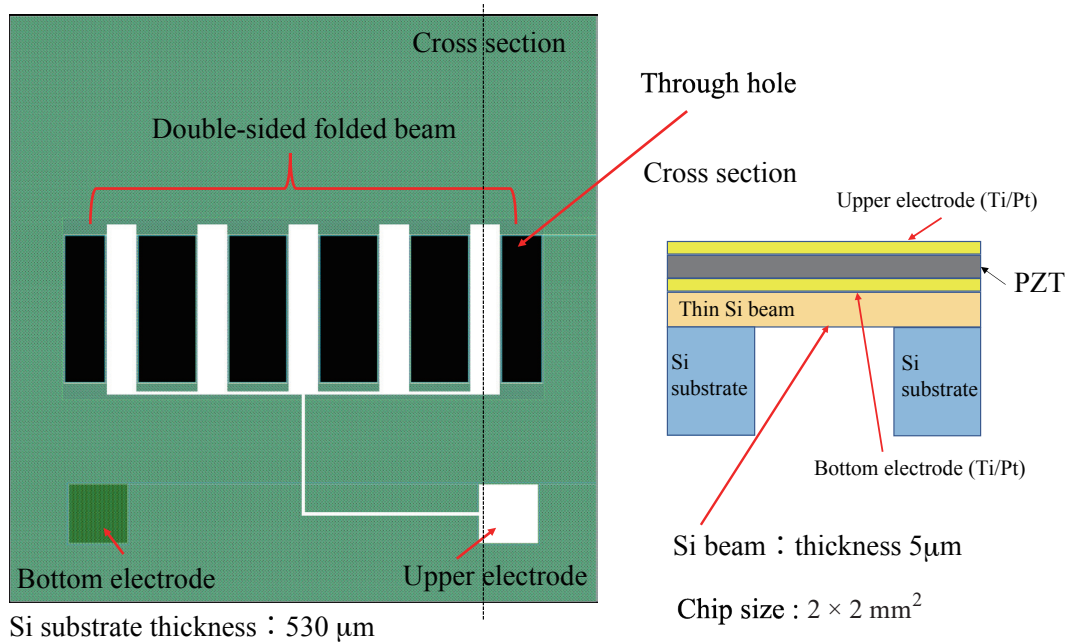

Fig. 3.   (Color online) Overview of a MEMS device with a double-sided beam structure. The substrate size is 2×2 mm^2. Multiple double-sided beams are arranged in a row, and when voltage is applied to the top and bottom electrodes, the beams bend to enable bending tests. A schematic of the MEMS cross-sectional shape with respect to the beam structure is shown in the inset.

Originally, an electrostatic actuator structure was frequently used, but a prototype was developed to determine whether an in-plane three-point tensile test structure based on an out-of-plane bending deformation element structure using lead zirconate titanate, $Pb(Zr, Ti)O_3$ (PZT), would be possible. There are two reasons: One is that there was an experimental report indicating that the electronic state of graphene can be significantly modulated by in-plane three-point tensile,[8,9] so we considered a device structure that can perform the in-plane three-point tensile test with a MEMS structure. The other was to fabricate the in-plane three-point tensile test device at the same time as a MEMS with a cantilever structure using PZT, which has been proven to be a driving source, in order to improve the efficiency of the process and device fabrication. Piezoelectric analysis (static analysis) was performed on the two designed device structures using a MEMS simulator, FEMTET.[31] The piezoelectric layer was divided into two layers with a mesh size of 5 μm. The lower electrode of the piezoelectric layer was set as GND and voltage was applied to the upper electrode. The aim of this study was to perform an in-plane tensile-compression test of the center using out-of-plane bending deformation with PZT. As shown in
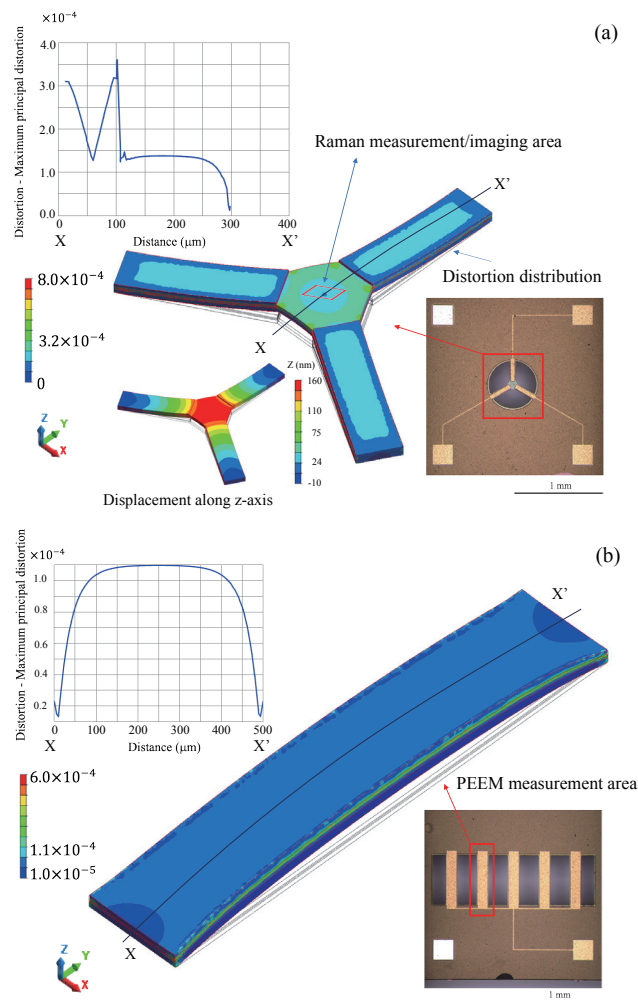

Fig. 4.   (Color online) Simulation results of strain evaluation for MEMS and optical photographs of prepared MEMS devices: (a) three-point tensile test type and (b) double-sided beam structure type. The spatial variation of distortion along the positions $X – X'$ is shown in each graph.

Fig. 4(a), the simulation results show that the center of the in-plane three-point tensile device has an almost constant height in the Z-direction, but the strain distribution spreads isotropically from the center with a spatial gradient in the in-plane direction. On the other hand, as an out-of-plane bending deformation element using PZT, simulation evaluation was also conducted for a double-sided symmetric folded-beam structure element. The results are shown in Fig. 4(b). As expected, the strain distributions related to out-of-plane bending deformation were obtained for the cantilever beam structure element. The same fabrication process was used to fabricate both devices by changing the lithography patterns.

MEMS devices that realize the three-point tensile test and double-sided symmetric folded-beam structures are prepared on a silicon substrate. Figure 1(b) shows a conceptual diagram of the structure of these MEMS devices exploited from the actual CAD data. The MEMS elements to be fabricated are 2×2 mm^2 in size and were constructed using multiple simultaneous semiconductor processes on a wafer. Figure 2 shows the structure of the MEMS device for the three-point tensile test. The beam structure with a thickness of 5 μm was configured at 120°, and thin film fabrication was performed on it using a sputtering system in the following configuration: bottom electrode (Ti/Pt)/thin PZT film/top electrode (Ti/Pt)/polyimide protective layer. The details of the fabrication procedure are described in Refs. 27–30. By applying voltage to the top and bottom electrodes (GND), a three-point tensile test can be performed. A schematic of the cross section near the center of the hole is shown in Fig. 2.

Similarly, a MEMS device with a double-sided symmetric folded-beam structure was constructed by changing the pattern using the same process. Figure 3 shows a schematic diagram. The device size is also 2×2 mm^2, with a beam structure of 5 μm thickness. Thin films were fabricated using a sputtering system, consisting of a bottom electrode, a PZT thin film, top electrode, and a polyimide protective film on top of the beam structure. By applying electrical pressure to the top and bottom electrodes, the PZT develops a piezoelectric effect, causing the beam structure to rise and fall while flexing.[27–30] Both optical photographs of the actual MEMS devices fabricated are shown in Figs. 4(a) and 4(b), respectively.

The purpose of this study is to confirm whether MEMS devices can be incorporated into synchrotron radiation analysis and micro-Raman spectroscopy systems. For the micro-Raman spectroscopy system, the three-point tensile-type MEMS device was fixed under the lens to prevent it from moving. As schematically illustrated in the inset of Fig. 5(a), the device was set and Raman spectra were measured at the center of the triangle beams. In particular, we will implement the device in an X-ray magnetic circular dichroism (XMCD) photoelectron emission microscopy (PEEM) system using a synchrotron radiation analysis system at BL17SU in SPring-8. Since the PEEM using soft X-rays also needs to operate in an ultrahigh-vacuum (UHV) apparatus, we will determine whether the MEMS devices can operate by introducing them into the system in which we have been conducting RF application and heating experiments.[32–35] In other words, a mechanical strain application mechanism using MEMS will be introduced as a novel experimental mechanism to the synchrotron radiation photoelectron spectroscopy microscopy system, which has an operando experimental environmental and is equipped with current and voltage application mechanisms.
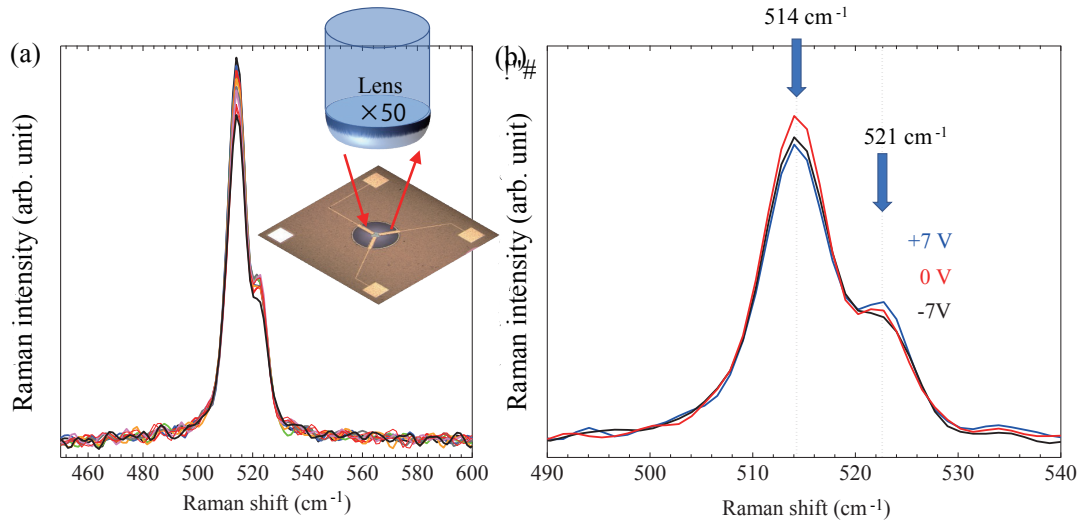
Fig. 5.   (Color online) Raman spectra at the central Si island of a three-point tensile test-type MEMS device. (a) Raman spectra measurement results over a wide range when electric voltages of +7, 0, and −7V were applied. (b) Raman spectra with extended Raman spectra shown in (a). The device and Raman spectroscopy arrangements are schematically shown in the inset.

3.   Results and Discussion

Before these operando experiments and analyses, we confirmed the operation of the MEMS device by introducing it into the micro-Raman spectrometer. First, to confirm the drive of the MEMS device by the Raman microscope, we determined whether the Raman shift caused by the distortion of the silicon beams could be observed or not. The center of the MEMS device for the three-point tensile test has an exposed silicon surface as shown in Fig. 4(a). The Raman spectrum was measured by focusing the objective lens (×50) of the microscopic Raman spectrometer at the center of three-point tensile devices illustrated schematically in Fig. 4(a). The measurement results are shown in Fig. 5. In the absence of strain in the crystal, the optical mode of Si (F2g mode) is triple degenerate with Raman activity, and only one Raman band is observed at 520 cm^{-1}.[36–39] Upon the application of uniaxial or biaxial stress, the triple degenerate modes are degenerate and split into singlet and doublet modes. In a backscattering configuration, only the LO mode, in which the atoms mutate in the <001> direction, is observed. That is, only the singlet mode corresponds to the mode observed at 514 cm^{-1}. When the strain ε is applied, the wavenumber shift $\Delta\omega$ for each Raman mode is known to be proportional to the strain. [36–39]

$$\Delta\omega = \omega - \omega_0 = b\varepsilon , \tag{1}$$

where ω and ω_0 are the Raman wavenumber obtained when the strain is applied and the original Raman wavenumber obtained in the absence of strain, respectively. The proportionality coefficient b for the LO mode is reported to be $b \sim 723 \pm 15$ cm^{-1}. Given a strain of 1×10^{-4}, a wavenumber change of about 0.7 cm^{-1} should be obtained. With the device design used in this

study, it is possible to give a strain of 1×10^{-4}, as shown in Figs. 2 and 3, but it is difficult to detect this wavenumber shift because the wavenumber resolution of the Raman spectrometer is a few cm^{-1}. However, since the spectral measurement is performed and the waveform changes in response to the MEMS device driven, it can be inferred that the Raman shift is caused by the added distortion. Originally, since distortion is added when the device is fabricated, a Raman band of 521 cm^{-1} without distortion and a Raman band of 514 cm^{-1} corresponding to the LO mode are detectable. Therefore, we will confirm that this system and the R&D direction are suitable for our purpose by observing how much the intensity ratio of the two changes when the device is driven.

As for the excitation laser wavelength and penetration depth, the wavelength of the laser source in our micro-Raman spectrometer was 785 nm, so the penetration depth into crystalline Si is considered to be about 10 μm. In this case, the thickness of the Si beam structure is 5 μm, so we can assume that we are observing the stress of the entire beam structure. On the other hand, when compressive stress is applied, the Raman lines shift to the high-wavenumber side. In Fig. 5, two Raman lines at 514 and 521 cm^{-1} are detected. The difference in Raman intensity between them indicates that tensile stress is applied. Figure 5(a) shows that there are only the earlier two Raman lines even when the measurement area is expanded. To measure the Raman spectral change in detail when voltage is applied to the MEMS device, the measurement area is expanded and the dependence of the Raman spectra on the application of voltage is compared in Fig. 5(b). In Fig. 5(b), it is clear that when voltage is applied to the MEMS device, the Raman lines shift slightly, but intensity changes occur. For each Raman shift, the voltage dependence of the intensity is shown in Fig. 6(a): the peak intensity at 521 cm^{-1} is almost independent of voltage, while the peak intensity at 514 cm^{-1} shows voltage dependence. To illustrate this point, the
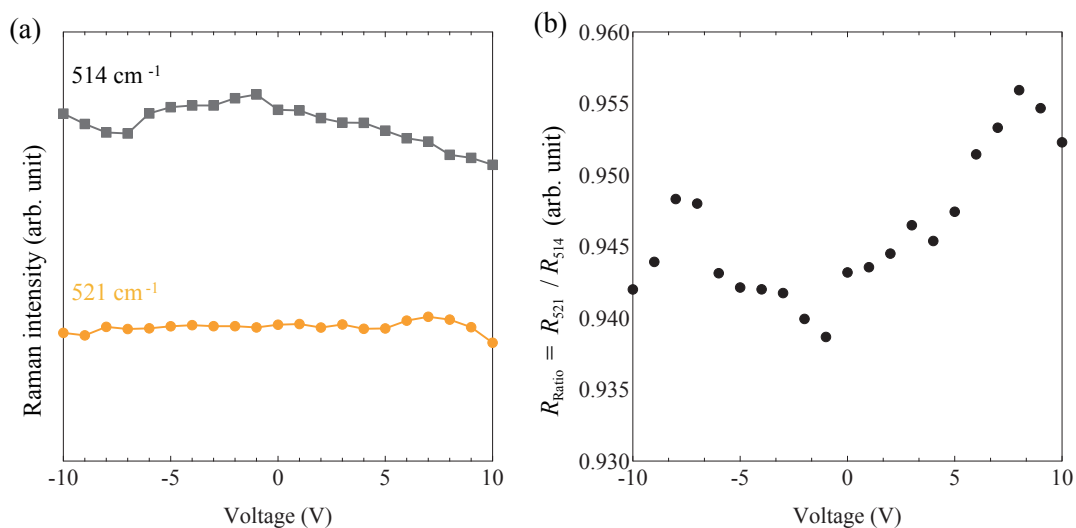

Fig. 6.   (Color online) (a) Electric voltage dependences of Raman intensities at 514 and 521 cm^{-1}. (b) Raman intensity ratio is defined as $R_r = R_{521}/R_{514}$, where R_{521} and R_{514} are the Raman intensities at 521 and 514 cm^{-1}, respectively.

voltage dependence of the Raman peak intensity, $R_{ratio} = R_{521}/R_{514}$, is shown in Fig. 6(b). It is found that the Raman intensity ratio increases with voltage when a positive voltage is applied.

Next, micro-Raman mapping was performed on the observed area, a 30×30 μm^2 region with a 1 μm step. Figures 7(a) and 7(b) show the peak mappings at 514 and 521 cm^{-1}, respectively. It can be seen that the spatial distribution of the Raman peak intensity changes with the application of voltage. This indicates that there is stress distribution within the silicon beam due to tensile stress caused by MEMS. In other words, the stress distribution is not uniform, indicating that there are local fluctuations. Probably, the origin is the spatial distribution of local strain during the device fabrication, i.e., the microfabrication and deposition of PZT and other films. After the device fabrication is finished, distortion due to its own weight and vibration during transportation may also generate strain distribution, although it is a very delicate structure.

From the above, it was found that tensile stress can be controlled by MEMS devices. Therefore, a basic experiment was conducted to introduce MEMS devices into a soft X-ray PEEM system. The experiment was conducted in the PEEM apparatus installed at BL17SU in SPring-8. In our previous studies,[32–35] a current electrode terminal for introducing microwaves was installed in this apparatus to directly observe the vortex swirling behavior of magnetic disks. In this study, we connected a MEMS device to this current electrode terminal to determine whether the MEMS device can operate in the UHV environmental state. Figure 8(a) shows a schematic setup of the MEMS device in the PEEM system with electrodes wired to the power source. Figure 8(b) shows an optical photograph of the MEMS element after it was wired to the sample holder of the PEEM apparatus with a double-sided beam-structure-type MEMS device.
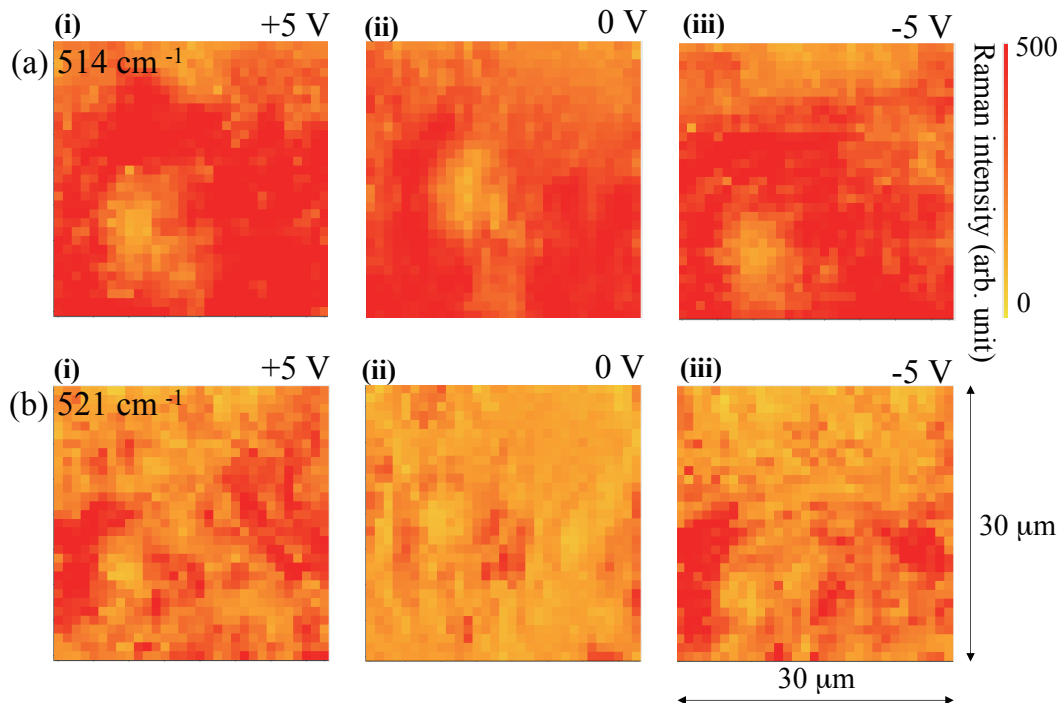

Fig. 7.   (Color online) Spatial distribution mappings of Raman peaks at (a) 514 and (b) 521 cm^{-1} when the electric voltages of (i) +5, (ii) 0, and (iii) −5 V were applied.
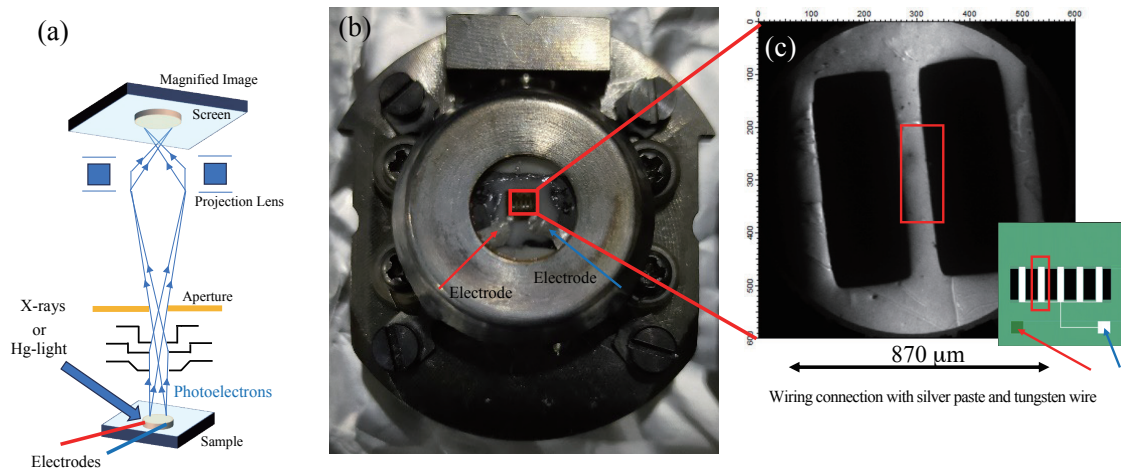
Fig. 8.   (Color online) (a) Schematic of device arrangement and PEEM observation setup. (b) Optical image of a double-sided beam-structure-type MEMS device after it is mounted in a PEEM holder at BL17SU in SPring-8. (c) PEEM observation image of a double-sided beam.

The center of the MEMS device has a double-sided beam structure, and the actual PEEM observation results at a low magnification are shown in Fig. 8(c). Next, Fig. 9(a) shows the PEEM observation image when a DC voltage of −5 V is applied to the double-sided beam structure-type MEMS device. The near-center position of the detector at which the PEEM image can be focused and observed clearly is read from the device settings. From the positional relationship between the detector and the sample surface, the displacement of the MEMS element due to bending stress is investigated. The distance between the detector and the sample surface is determined to be 1.84 mm when the detector is focused as shown in Fig. 9(a). Next, when the voltage is changed to 0 V, the focus is displaced. Figure 9(b) shows the PEEM observation image obtained before focusing when the voltage is set to 0 V. Comparing Fig. 9(a) with Fig. 9(b), we found that the focus was clearly shifted. The out-of-focus observation image was refocused by controlling the distance between the detector and the sample surface so that the PEEM observation image became clear again; the detector position when the PEEM observation image was in focus was read as 1.93 mm. This process was performed while varying the voltage applied to the MEMS device, and the voltage dependence of the distance between the sample surface and the detector is shown in Fig. 9(c). The voltage dependence of the distance between the sample surface and the PEEM detector indicates that there is some hysteresis when a positive voltage is applied. However, the results show that the bending displacement of the MEMS device's cantilever beam changes almost linearly, indicating that the displacement of about 200 μm can be controlled when the voltage is increased from −5 to +5 V. The above results show that the MEMS device works as expected in the UHV environmental experimental state.

By using MEMS devices, we found that PEEM observation and micro-Raman spectroscopic mapping can be performed while conducting tensile stress tests, even with small sample sizes. The system can be operated in vacuum and can be applied to synchrotron radiation analysis using soft X-rays. Using this system, we were able to construct an environment in which the

(a) DC: -5V   (b) DC: 0V   (c)

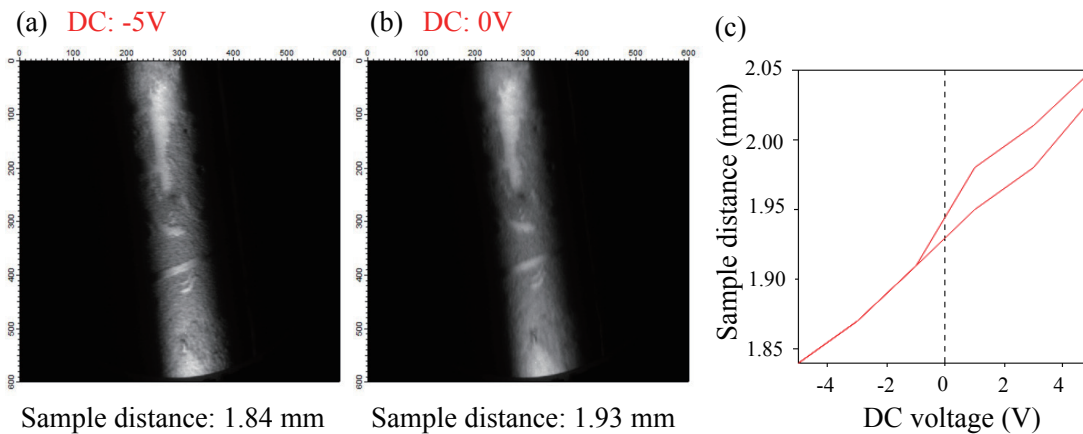Sample distance: 1.84 mm   Sample distance: 1.93 mm

Fig. 9.   (Color online) PEEM observation of a single beam of a double-sided beam-structure-type MEMS device. (a) PEEM image of the single beam when focusing at an electric voltage of −5 V applied to the MEMS device. The distance between the sample surface and the PEEM detector was 1.84 mm. (b) PEEM image when the electric voltage was set to 0 V. The image is not focused at this time and is unclear. The distance between the sample surface and the PEEM detector was adjusted to obtain a clear PEEM image. Then, the distance was 1.93 mm. The distance when the electric voltage was applied to the MEMS device was changed by repeating this operation. By measuring this distance, the operating range of the beam when the electric voltage is applied to the MEMS device can be examined. The data obtained in this way are summarized in (c), indicating the electric voltage dependence of the distance.

electronic and chemical states of a sample mounted on a MEMS device or an adhesive interface can be directly measured while mechanically modulating the state of the sample.

4.   Conclusion

To investigate the chemical and electronic states of a sample when mechanical strain is applied, basic introduction experiments were conducted on the electrically controlled mechanical stress application mechanism using MEMS devices. We succeeded in introducing a three-point tensile MEMS device and a double-sided beam structure MEMS device, both of which are driven by PZT. In combination with micro-Raman spectroscopy, we succeeded in detecting the Raman signal change by tensile testing in the region where the silicon beams of the MEMS device were exposed. We also succeeded in introducing the MEMS device into an ultrahigh-vacuum chamber and demonstrated that the system can be combined with PEEM observation. This system is expected to provide a procedure to quantitatively and systematically evaluate mechanical stress changes in chemical and electronic states in the adhesive region, as well as chemical state changes in polymer materials and other materials due to the application of stress.

Acknowledgments

References

1   A. K. Geim: Science **324** (2009) 1530.
2   M. Z. Hasan and C. L. Kane: Rev. Mod. Phys. **82** (2010) 3045.
3   W. Wei, E. Pallecchi, M. Belhaj, A. Centeno, Z. Amaia, D. Vignaud, and H. Happy: Proc. 2016 11th European Microwave Integrated Circuits Conference (EuMIC, 2016) 165–168 https://doi.org/10.1109/EuMIC.2016.7777516.
4   E. Guerriero, P. Pedrinazzi, A. Mansouri, O. Habibpour, M. Winters, N. Rorsman, A. Behnam, E. A. Carrion, A. Pesquera, A. Centeno, A. Zurutuza, E. Pop, H. Zirath, and R. Sordan: Sci. Rep. **7** (2017) 2419.
5   Graphene Field effect transistors (GFETS) are commercially sold. For example, https://www.sigmaaldrich.com/JP/ja/technical-documents/technical-article/materials-science-and-engineering/biosensors-and-imaging/graphene-fet-chip
6   Y. Yamashita, A. Endoh, K. Shinohara, K. Hikosaka, T. Matsui, S. Hiyamizu, and T. Mimura: IEEE Electron Device Lett. **23** (2002) 573.
7   D. L. Harame J. H. Comfort, J. D. Cressler, E. F. CrabbC, J. Y.-C. Sun, B. S. Meyerson, and T. Tice: IEEE Trans. Electron Devices **42** (1995) 455.
8   K. K Gomes, Warren Mar, W. Ko, F. Guinea, and H. C. Manoharan: Nature **483** (2012) 306.
9   G. López-Polín, C. Gómez-Navarro, V. Parente, F. Guinea, M. I. Katsnelson, F. Pérez-Murano, and J. Gómez-Herrero: Nat. Phys. **11** (2015) 26.
10 A. Yamaguchi, A. Hirohata, and B. J. H. Stadler: Nanomagnetic Materials: Fabrication, Characterization and Application (Elsevier, Amsterdam, 2021).
11 A. Yamaguchi, T. Ohkochi, M. Oura, K. Yamada, T. Saiki, S. Suzuki, Y. Utsumi, and A. Nakao: Nanomaterials **11(4)** (2021) 1021.
12 R. Nakamura, S. Saegusa, N. Akamatsu, K. Yamada, T. Ogasawara, M. Oura, T. Ohkochi, and A. Yamaguchi: Jpn. J. Appl. Phys. **60** (2021) SBBC01.
13 M. Ito, S. Ono, H. Fukui, K, Kogirima, N. Maki, T. Hikage, T. Kato, T. Ohkochi, A. Yamaguchi, M. Shima, and K. Yamada: J. Magn. Magn. Mater. **564** (2022) 170177.
14 D. Mukhopadhyay, D. A. Walko, I. W. Jung, C. P. Schwartz, J. Wang, D. López, and G. K. Shenoy: Nature Commun. **6** (2015) 7057.
15 D. S. Grierson, A. R. Konicek, G. E. Wabiszewski, A. V. Sumant, M. P. de Boer, A. D. Corwin, and R. W. Carpick: Tribol. Lett., **36** (2009) 233.
16 T. Namazu, Y. Isono, and T. Tanaka: Proc. IEEE Thirteenth Annu. Int. Conf. Micro Electro Mechanical Systems (Cat. No.00CH36308, Miyazaki, Japan, 2000) 205–210. https://doi.org/10.1109/MEMSYS.2000.838517.
17 T. Namazu: IEEJ Trans. Electr. Electron. Eng. **18** (2023) 308.
18 K. Fujitani, Y. Utsumi, A. Yamaguchi, H. Sumida, and S. Suzki: Appl. Surface Sci. **637** (2023) 157891.
19 K. Fujitani, K. Tanaka, K. Takahara, H. Sumida, A. Yamaguchi, Y. Utsumi, and S. Suzuki: Heliyon **9** (2023) e15794.
20 S. Araki, R. Settai, T. C. Kobayashi, H. Harima, and Y. Onuki: Phys. Rev. B: Condens. Matter **64** (2001) 224417.
21 C. S. Garde, F. Honda, R. Settai, Y. Onuki: J. Phys. Soc. Jpn. **77** (2008) 356.
22 J. Shin, T. W. Cornelius, S. Labat, F. Lauraux, M. -I. Richard, G. Richer, N. P. Blanchard, D. S. Gianola, and O. Thomas: J. Appl. Cryst. **51** (2018) 781.
23 A. Yamaguchi, S. Ikeda, M. Nakaya, Y. Kobayashi, Y. Haruyama, S. Suzuki, K. Kanda, Y. Utsumi, H. Sumida, and M. Oura: J. Electron. Spectrosc. Relat. Phenom. **267** (2023) 147385.
24 A. Yamaguchi, N. Akamatsu, S. Saegusa, R. Nakamura, M. Kata, I. Yagi, I. Ishihara, and M. Oura: RSC Adv. **12** (2022) 10425.
25 S. Lou, J.-Y. Ye, K.-Q. Li, and A. Wu: Analyst **137** (2012) 1174.
26 A. Yamaguchi, R. Takahashi, T. Fukuoka, R. Hara, and Y. Utsumi: Sens. Actuators, B **230** (2016) 94.

27 K. Kanda, T. Okubo, M. Shima, T. Fujita, and K. Maenaka: IEEJ Trans. Sens. Micromach. **137** (2017) 284.
28 K. Kanda, S. Toyama, K. Takahara, T. Fujita, and K. Maenaka: IEEJ Trans. Sens. Micromach. **139** (2019) 369.
29 K. Kanda, K. Takahara, S. Toyama, T. Fujita, and K. Maenaka: Jpn. J. Appl. Phys. **57** (2018) 11UF14.
30 K. Kanada, T. Aiba, and K. Maenaka: Sens. Mater. **34** (2022) 1879.
31 Femtet: https://www.muratasoftware.com (accessed 15 August 2024).
32 T. Ohkochi, A. Yamaguchi, M. Kotsugi, H. Hata, M. Goto, Y. Nozaki, T. Nakamura, H. Oiwa, and T. Kinoshita: Jpn. J. Appl. Phys. **51** (2012) 128001.
33 T. Ohkochi, M. Tanaka, T. Ohtuski, Z. Horita, F. Kitajima, A. Yamaguchi, M. Kotsugi, H. Ogawa, and M. Oura: J. Electron. Spectrosc. Relat. Phenom. **267** (2023) 147371.
34 T. Ohkohchi, H. Osawa, A. Yamaguchi, H. Fujiwara, and M. Oura: Jpn. J. Appl. Phys. **58** (2019) 118001.
35 A. Yamaguchi, H. Hata, T. Ohkochi, M. Goto, M. Kodama, Y. Kasatani, K. Sekiguchi, Y. Nozaki, M. Kotsugi, and T. Kinoshita: Jpn. J. Appl. Phys. **55** (2016) 023002-1-13.
36 R. Loudon: Adv. Phys. **13** (1964) 423.
37 H. J. Mcskimin, W. L. Bond, E. Buehler, and G. K. Teal: Phys. Rev. **83** (1951) 1080.
38 H. Miura, H. Ohta, H. Sakata, and N. Okamoto: Jpn. Soc. Mech. Eng. Int. J. Ser.A: **36** (1993) 302.
39 S. Nakashima, T. Mitani, and M. Yoshikawa: Oyo Buturi **75** (2006) 1224. https://doi.org/10.11470/oubutsu.75.10_1224